# Supporting Information

# High-precision synthesis of α-$MnO_2$ nanowires with controllable crystal facets for propane oxidation

*Chao Feng[1], Gaoyan Xiong[1], Yaping Li[2], Qianqian Gao[1], Yuan Pan[1,*], Zhaoyang Fei[3], Yanpeng Li[1], Yukun Lu[2], Chenguang Liu[1] and Yunqi Liu[1,*]*

[1] State Key Laboratory of Heavy Oil Processing, College of Chemical Engineering, China University of Petroleum, Qingdao 266580, China

[2] College of Science, China University of Petroleum, Qingdao 266580, China

[3] State Key Laboratory of Materials-Oriented Chemical Engineering, Nanjing Technology University, Nanjing 211816, China

* E-mail: panyuan@upc.edu.cn (Y. Pan); liuyq@upc.edu.cn (Y. Liu)

Summary of the supporting information: 22 pages, 6 tables and 12 figures

# Catalyst Characterization.

Transmission electron microscopy (TEM), high-resolution transmission electron microcopy (HRTEM) images and Energy-dispersive X-ray spectroscopy (EDS) elemental mapping images were collected on a JEM-2100UHR instrument at a voltage of 200 kV. The as-prepared samples were firstly treated by ultrasonic dispersion in ethanol and then dried on a carbon film supported by a copper grid.

The XRD patterns were obtained by X' Pert Pro MPD between 25° and 85° at a step length of 5° $min^{-1}$ with a Cu Kα radiation (λ = 0.154056 nm). The crystalline sizes of catalysts were estimated by the Scherrer formula which was showed below (eq 1):

$$D = \frac{K\lambda}{B\cos\theta} \qquad (1)$$

K is the Scherrer constant "0.89", when B is the half-width of X-ray diffraction; θ is diffraction angle.

The $N_2$ adsorption-desorption isotherm, BET surface area, t-plot area, pore size and pore volume of the catalysts were measured at 77 K with a Micromeritics ASAP2010 instrument, used the Barrett-Joyner-Halenda (BJH) method. Before the test, each sample was pretreated at 573 K for 2 h under 7-10 mmHg. Elemental analysis was performed by inductively coupled plasma-atomic emission spectroscopy (ICP-AES) on an Agilent ICPOES 730.

The Scanning Electron Microscope (SEM) images were recorded on a Hitachi S-4800 apparatus at a voltage of 200.0 kV.

The XPS patterns were measured on a Escalab 250 Xi electronic energy spectrum at 300 W using Mg Kα X-rays as the excitation source. The data were processed by the XPS-PEAK software,

and surface element contents were calculated through XPS peak areas. The Binding energies (BE) were calibrated by the C 1s at 284.8 eV.

$H_2$ temperature programmed reduction ($H_2$-TPR) and $O_2$ temperature programmed desorption ($O_2$-TPD) were operated on a Quantachchrome Chembet Pulsar apparatus with the same pretreatment. Briefly, 100 mg samples with 40-60 mesh were pretreated at 300 ℃ for 70 min under Helium in the U-shape quartz reactor. For $H_2$-TPR, the samples were first cooled down to 30 ℃, then reacted with Hydrogen from 50 ℃ to 750 ℃ with a heating rate of 10 ℃ $min^{-1}$ under the atmosphere of 10 % $H_2$/He (50 mL·$min^{-1}$). And for $O_2$-TPD, after cooling under Helium, the samples were treated by a 5 % $O_2$/$N_2$ gas flow (50 mL·$min^{-1}$) for $O_2$ adsorption and saturation, then the samples were heated from 50 to 600 ℃ under the atmosphere of He (50 mL·$min^{-1}$) with a heating rate of 10 ℃·$min^{-1}$.

The Fourier Transform Infrared spectroscopy analysis of the catalyst adopts the American Nicolet NEXUS Fourier Transform Infrared Spectrometer. Weigh a certain amount of KBr particles and catalysts, grind them into powder in an agate mortar, and put them into an infrared spectrometer for testing after pressing.

Raman spectra were collected on a ThermoFisher DXR microscope with 532 nm laser excitation.

Electron paramagnetic resonance spectra were collected on a Bruker A300 spectrometer. The spectrometer operates at microwave frequency near 100 kHz. Oxford helium cryostat enabled measurement from room temperature down to 3560. Simulations were performed with Bruker WinEPR Simphonia. The concentration were estimated by comparing the integral intensity of signal.

*In-situ* DRIFT spectra were obtained on a Bruker Equinox 55 instrument equipped with an MCT/A detector and a ZnSe *in-situ* cell. The spectra were collected by accumulating 64 scans with

a resolution of 4 $cm^{-1}$. Prior to each test, the sample was pretreated by heated at 80 ℃ for 6 h, and then cooled down to room temperature for further reaction.

# Electrochemical measurement.

A Gamry Reference 3000 in a classic 3-electrode mode was utilized to carry out the electrochemical impedance spectroscopy (EIS) measurements. The counter electrode was a graphite rod, the reference electrode was an Ag/AgCl (saturated KCl), and the working electrode was a glassy carbon electrode (GCE) modified with the sample. The working electrode was prepared as follows: The as-fabricated sample (5.0 mg) was dispersed into ethanol (450 μL) and deionized water (500 μL) mixed with Nafion (50 μL) at a 5% (w/w) ratio. The suspension was subjected to 30-min of ultrasonication to produce a homogeneous ink. 5 μL of the ink was then spread onto a 3-mm-diameter polished GCE. Prior to obtaining the data, the GCE was dried for 1 h at ambient temperature to yield a mass loading of 0.35 $mg \cdot cm^{-2}$. The EIS test was conducted at a –0.40 V (overpotential) over a frequency range of $10^5$–$10^{-2}$ Hz against the reference electrode.

# Reaction Kinetics Measurement

The $C_3H_8$ conversion ($X_{C_3H_8}$) and TOF were calculated with the eqs 2 and 3.

$$X_{C_3H_8} = \frac{[C_3H_8]_{inlet} - [C_3H_8]_{outlet}}{[C_3H_8]_{inlet}} \times 100\% \quad (2)$$

$$TOF = \frac{[C_3H_8]_{inlet} \times X_{C_3H_8} \times V}{[Mn^{4+}]} \quad (3)$$

where $[C_3H_8]_{inlet}$ and $[C_3H_8]_{outlet}$ are the $C_3H_8$ concentrations in the inlet and outlet gas (vol.%), respectively. $[Mn^{4+}]$ was the concentration of the active $Mn^{4+}$ over the catalysts obtained by the

results of XPS (mol). And V in the total flow rate (mol·s$^{-1}$), the reaction rate, $r_{C3H8}$ (mol·$g_{MnOx}^{-1}$ s$^{-1}$), is calculated with $X_{C3H8}$ as the eq 4:

$$r_{C_3H_8} = \frac{N_{C_3H_8} \cdot X_{C_3H_8}}{W_{cat} \cdot w\%_{MnO_x}} \quad (4)$$

where $N_{C3H8}$ is the $C_3H_8$ gas flow rate (mol·s$^{-1}$), $W_{cat}$ is the catalyst weight (g), $w\%_{MnOx}$ is the content of $MnO_2$.

When the conversion of propane is lower than 20 %, a dependence of the reaction rate ($r_{C3H8}$) on the products of $CO_2$ and $H_2O$ can be ignored. Therefore, the empirical kinetic expression of the reaction rate equation can be described as eq 5:

$$r_{C_3H_8} = A\, exp\left(-\frac{E_a}{RT}\right) P_{C_3H_8}^{\alpha} P_{O_2}^{\beta} \quad (5)$$

Then taking the logarithm of eq 4, we get eq 6.

$$\ln r_{C_3H_8} = -{E_a}/{RT} + \ln A + \alpha ln\, P_{C_3H_8} + \beta \ln P_{O_2} \quad (6)$$

When the conversion of propane is lower than 20 %, the components of the reactant feed gas variation can be ignored. Hence ln A, αln $P_{C3H8}$ and βln $P_{O2}$ can be supposed to be approximately constant, and eq 6 can be simplified to eq 7.

$$\ln r_{C_3H_8} = -{E_a}/{RT} + C \quad (7)$$

The activation energy ($E_a$) can be obtained from the slope of the resulting linear plot of ln r versus 1/T.

# Density functional theory (DFT) Calculation Details

In the calculation of oxygen vacancy formation energy, the slab model surfaces of $MnO_2$ were built. A p (2×2) unit cell expansion is used to model. A vacuum of 10 Å was used to simulate the surface in periodic boundary condition.

The energy of oxygen vacancy formation, $E_v$, for an oxygen atom released from $MnO_2$ on the surface to generate an oxygen vacancy is defined as (eq 8):

$$E_v = E_{defect} + \mu_O - E_{bulk} \quad (8)$$

where $E_{bulk}$ is the total clean relaxation energy of the surface slab, $\mu_O$ is the chemical potential of oxygen, and $E_{defect}$ is the total energy of the slab with an oxygen atom removed from the surface. Since the calculations are performed a t 0 K and fixed cell volume, the differences in Gibbs free energy should equal the differences in total energy. By this definition, the lower the $E_v$ is, .the easier oxygen ions will be released, which will promote the migration of oxygen atoms surrounded.

The binding energy (Eads) of propane molecule on the surface were calculated as (eq 9):

$$E_{ads} = E_{adsorbate+surface} - E_{surface} - E_{gas} \quad (9)$$

where $E_{surface}$ is the clean surface relaxation energy of the surface slab, $E_{gas}$ is the energy of a free gas molecules in the vacuum, and $E_{adsorbate+surface}$ is the energy of the composite system. Because of the calculations are performed at 0 K and fixed cell volume, the differences in Gibbs free energy should equal the differences in total energy. By this definition, a negative value of $E_{ads}$ corresponds to exothermic and spontaneous adsorption processes.

# Figures

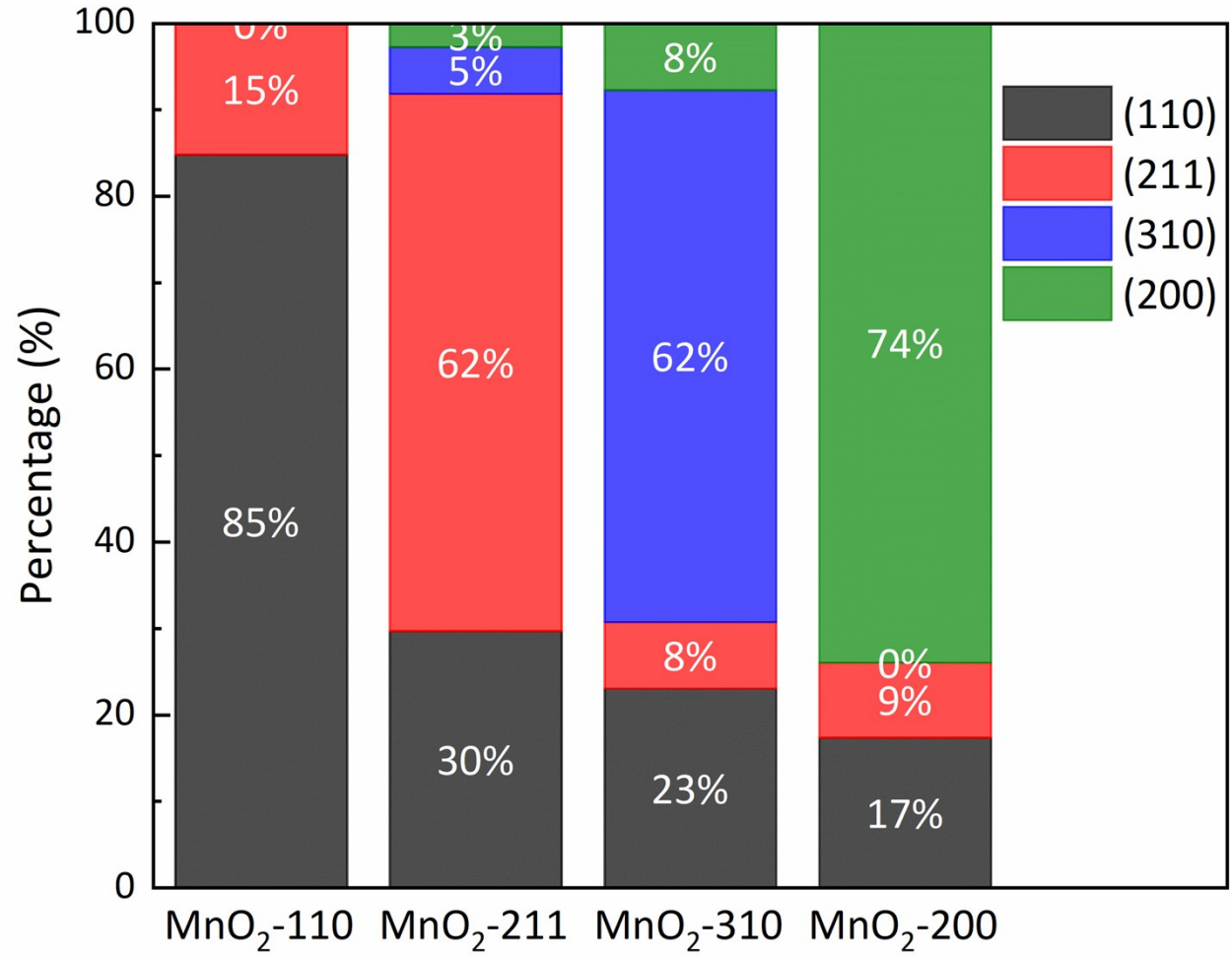


**Figure S1.** Percentage of different crystal planes of α-$MnO_2$ nanowire catalysts.

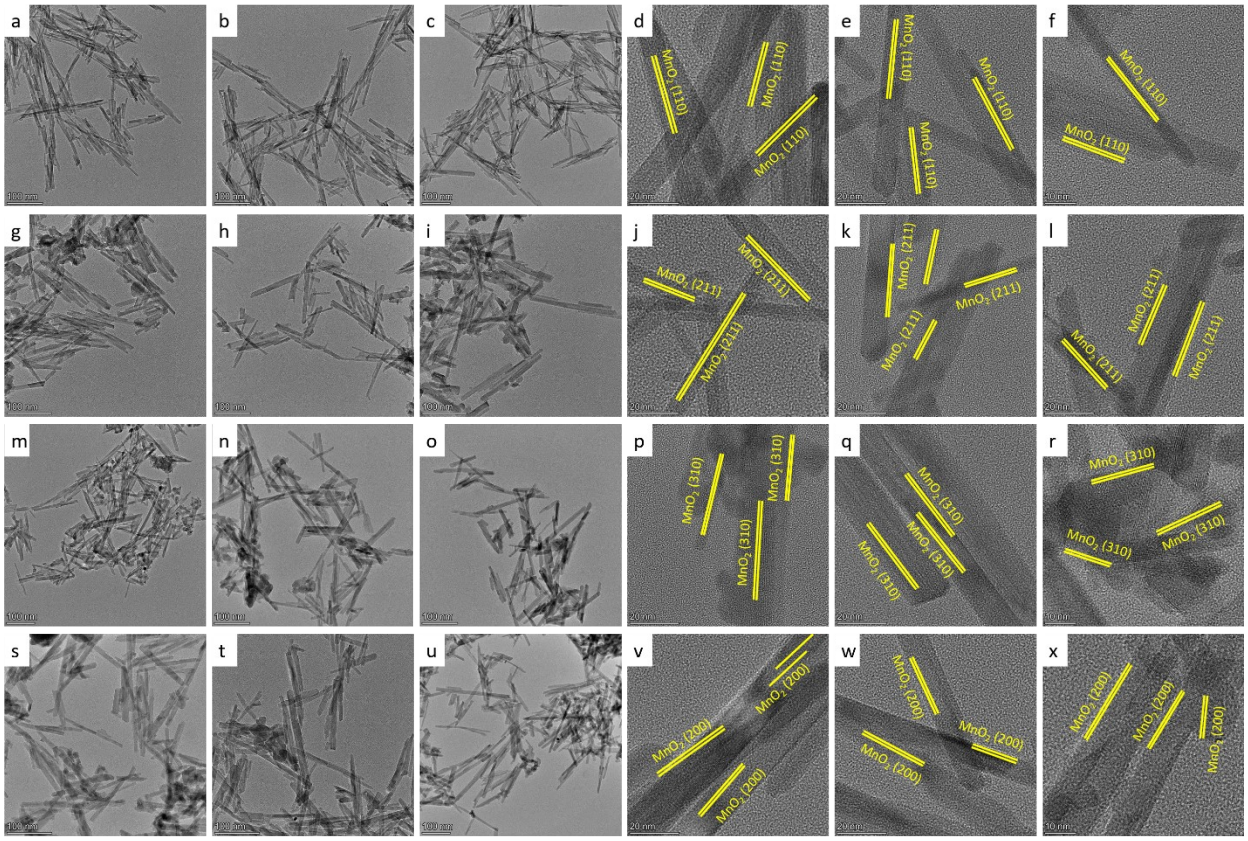


**Figure S2.** TEM and HRTEM of (a-f) $MnO_2$-110, (g-l) $MnO_2$-211, (m-r) $MnO_2$-310, (s-x) $MnO_2$-200 catalysts.

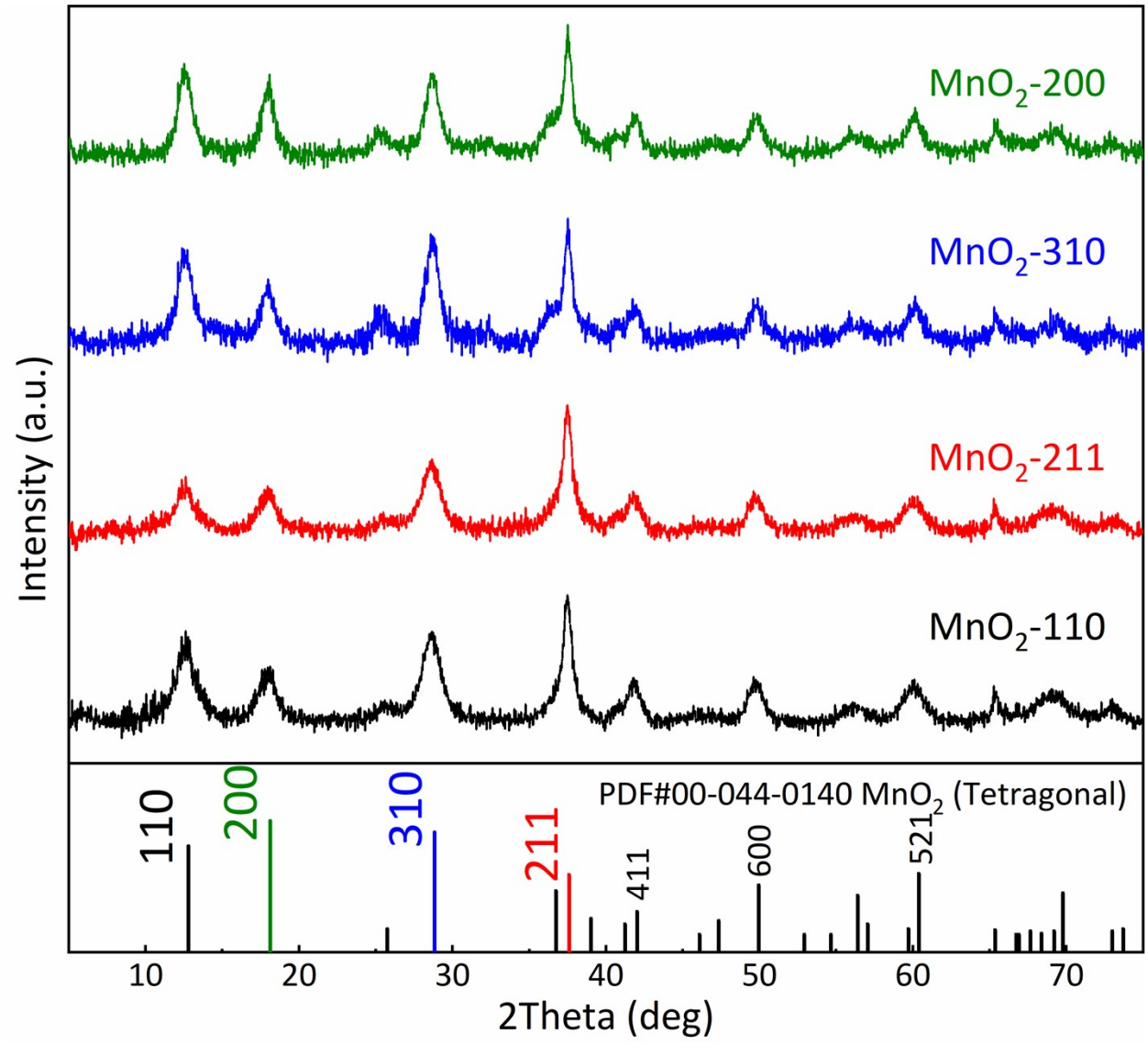


**Figure S3.** Powder XRD patterns of fresh α-$MnO_2$ nanowire catalysts with different facets.

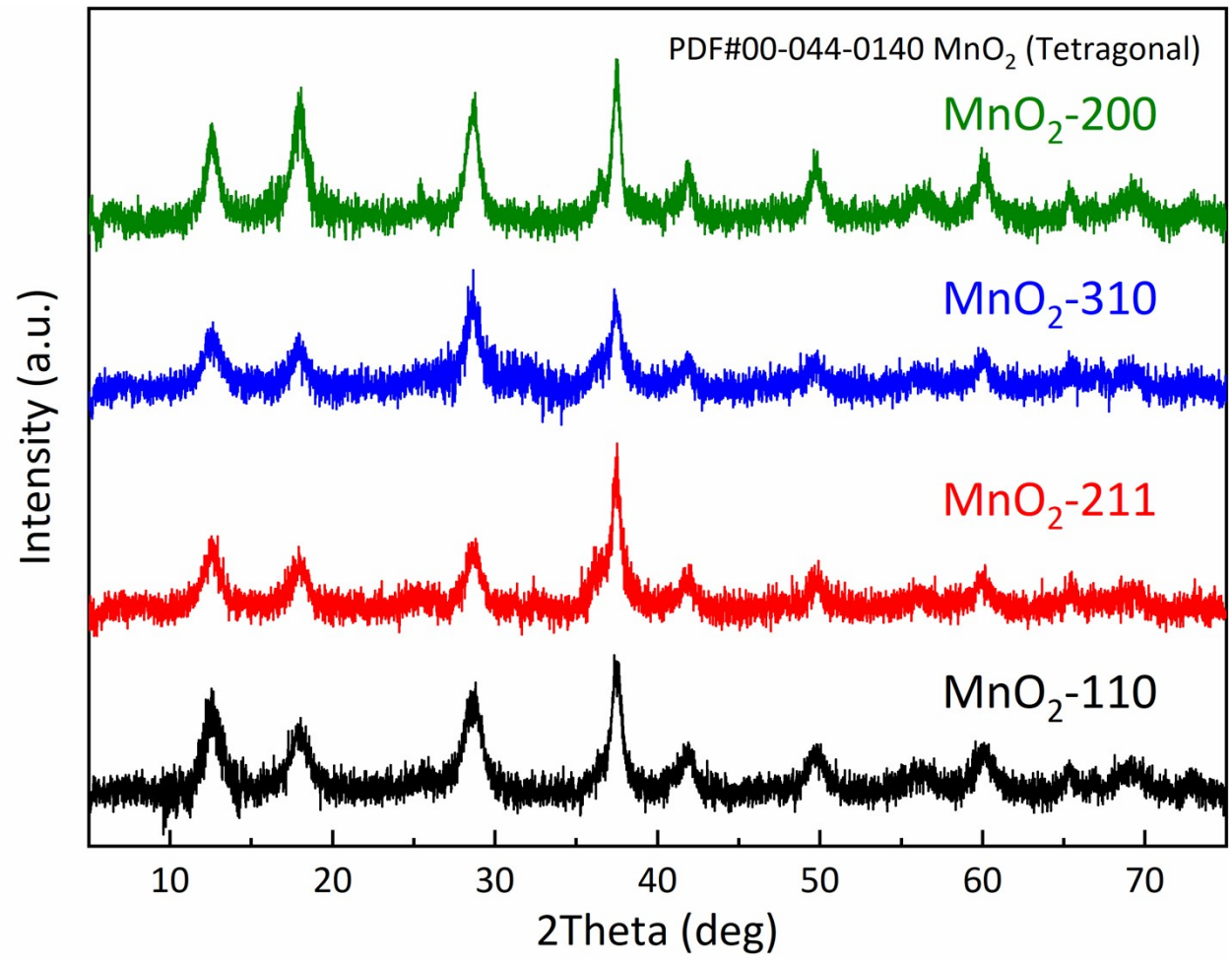


**Figure S4.** Powder XRD patterns of used α-$MnO_2$ nanowire catalysts at $T_{50}$ of reaction.

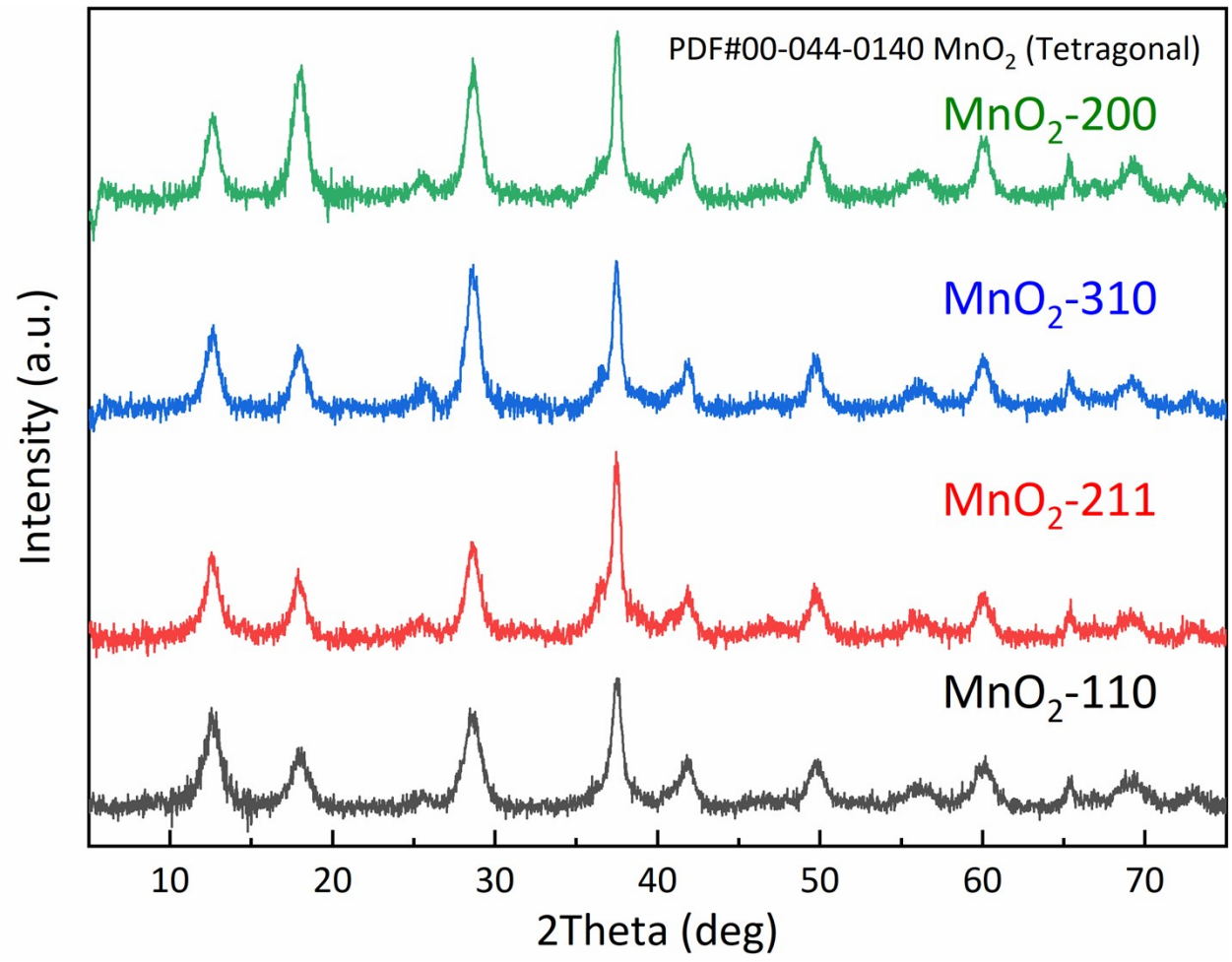


**Figure S5.** Powder XRD patterns of used α-$MnO_2$ nanowire catalysts after reaction.

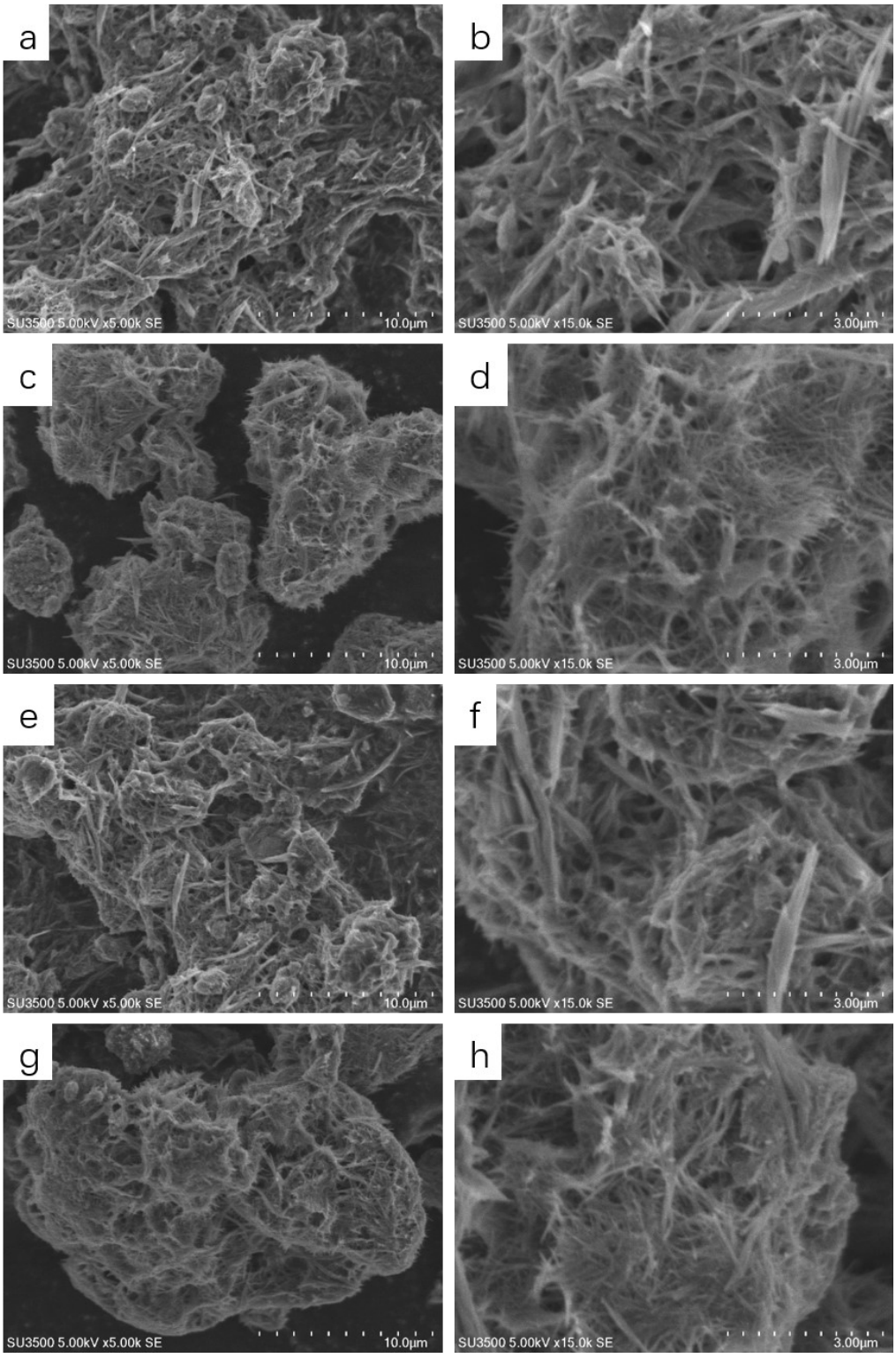


**Figure S6.** SEM images of (a)(b) $MnO_2$-110, (c)(d) $MnO_2$-200 before reaction and (e)(f) $MnO_2$-110, (g)(h) $MnO_2$-200 after reaction.

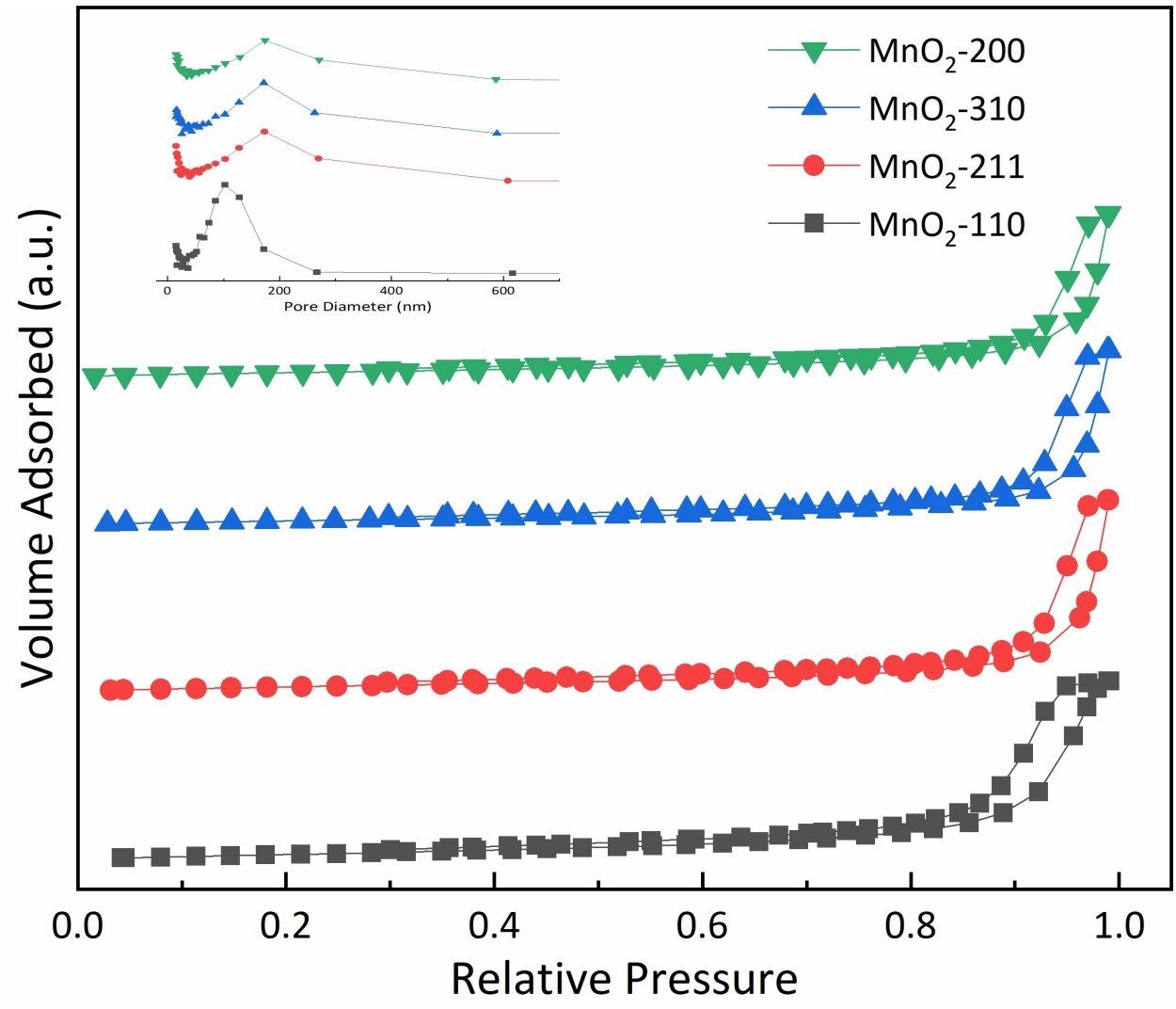


**Figure S7.** $N_2$ adsorption-desorption isotherm and pore size distributions of α-$MnO_2$ nanowire catalysts.

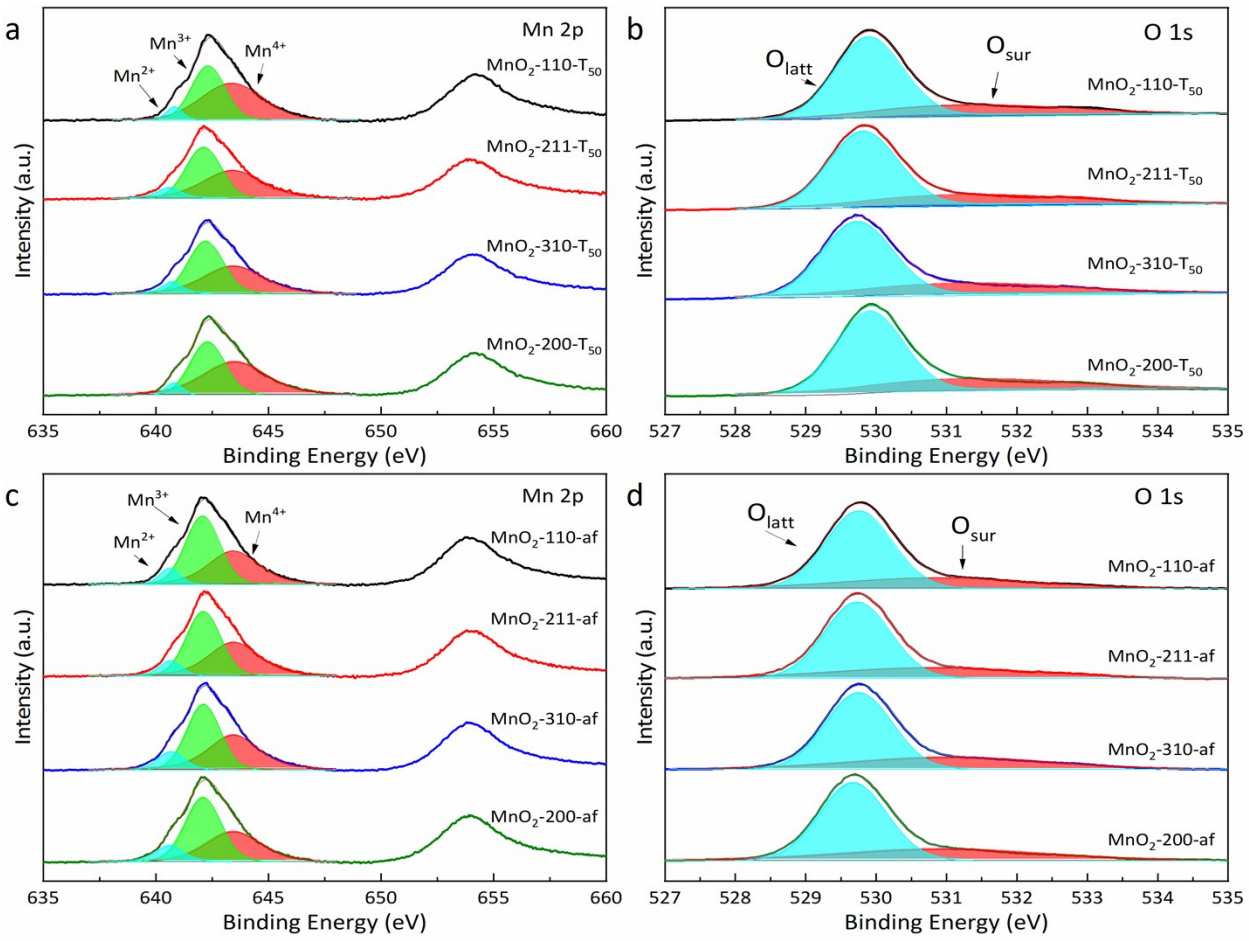


**Figure S8.** Mn 2p and O 1s XPS spectra for α-$MnO_2$ nanowire catalysts (a) (b) at $T_{50}$ of reaction, (c) (d) after reaction.

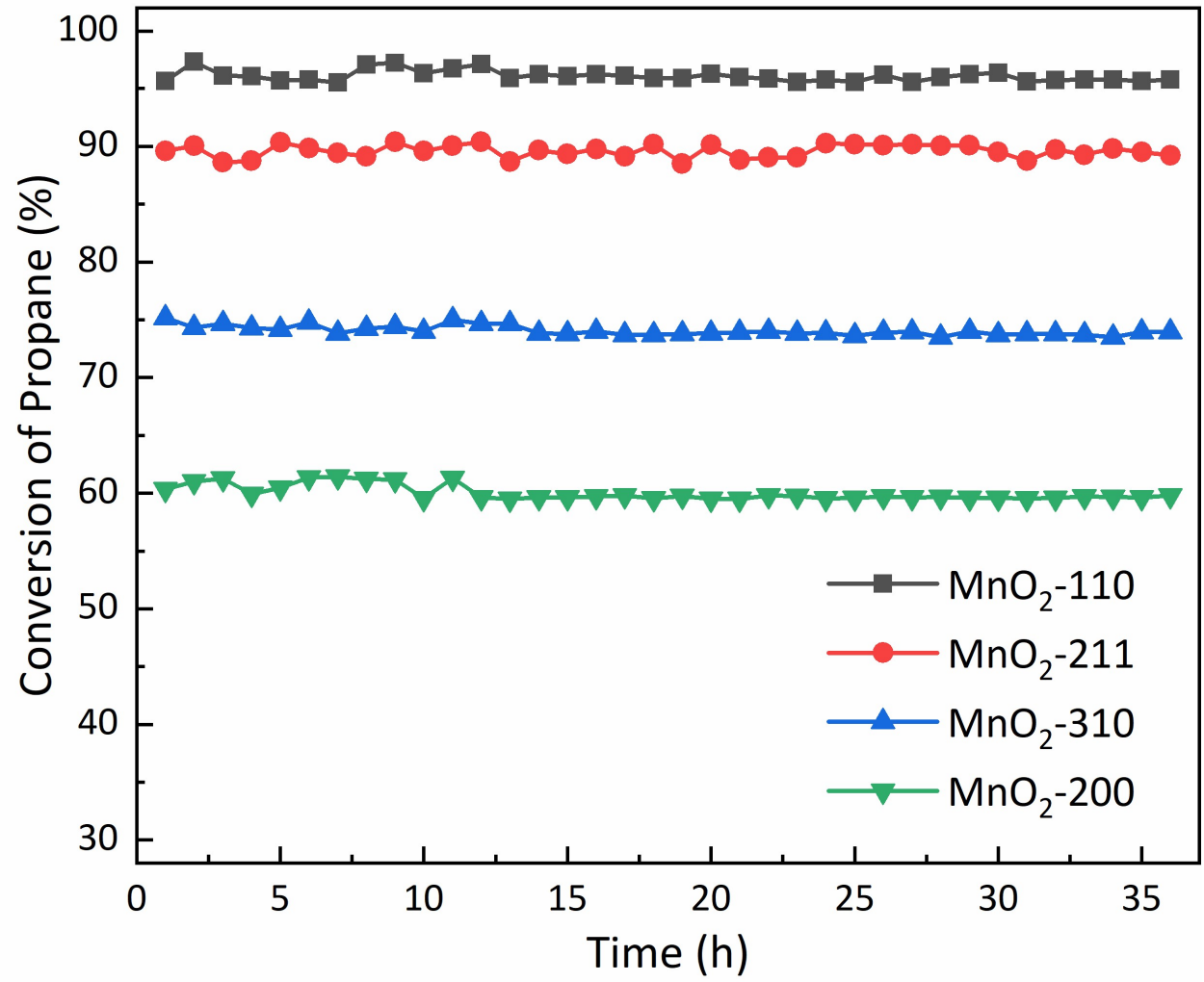


**Figure S9.** Catalytic stability of α-$MnO_2$ nanowire catalysts at 275 ℃.

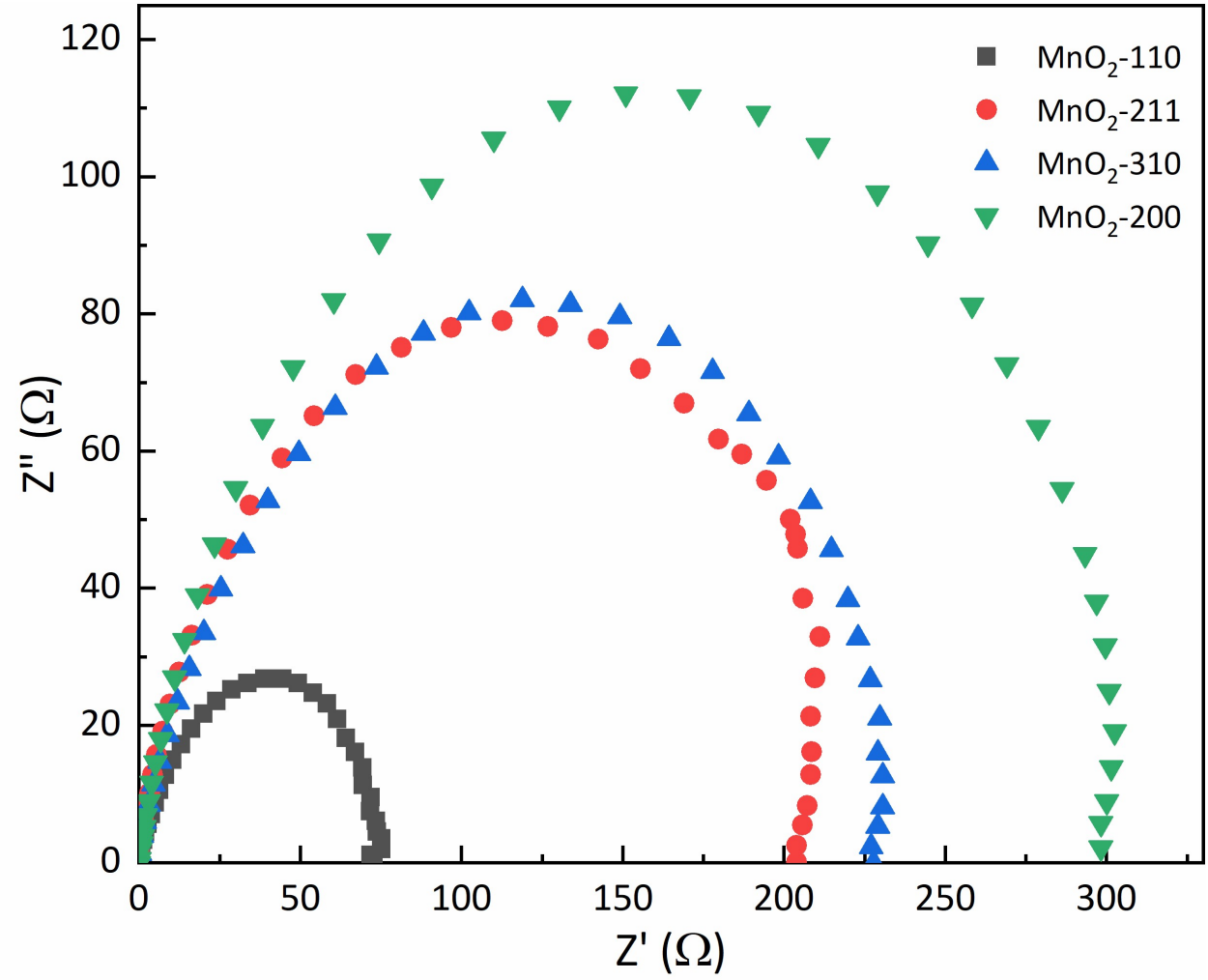


**Figure S10.** Electrochemical impedance spectroscopy (EIS) data for α-$MnO_2$ nanowire catalysts.

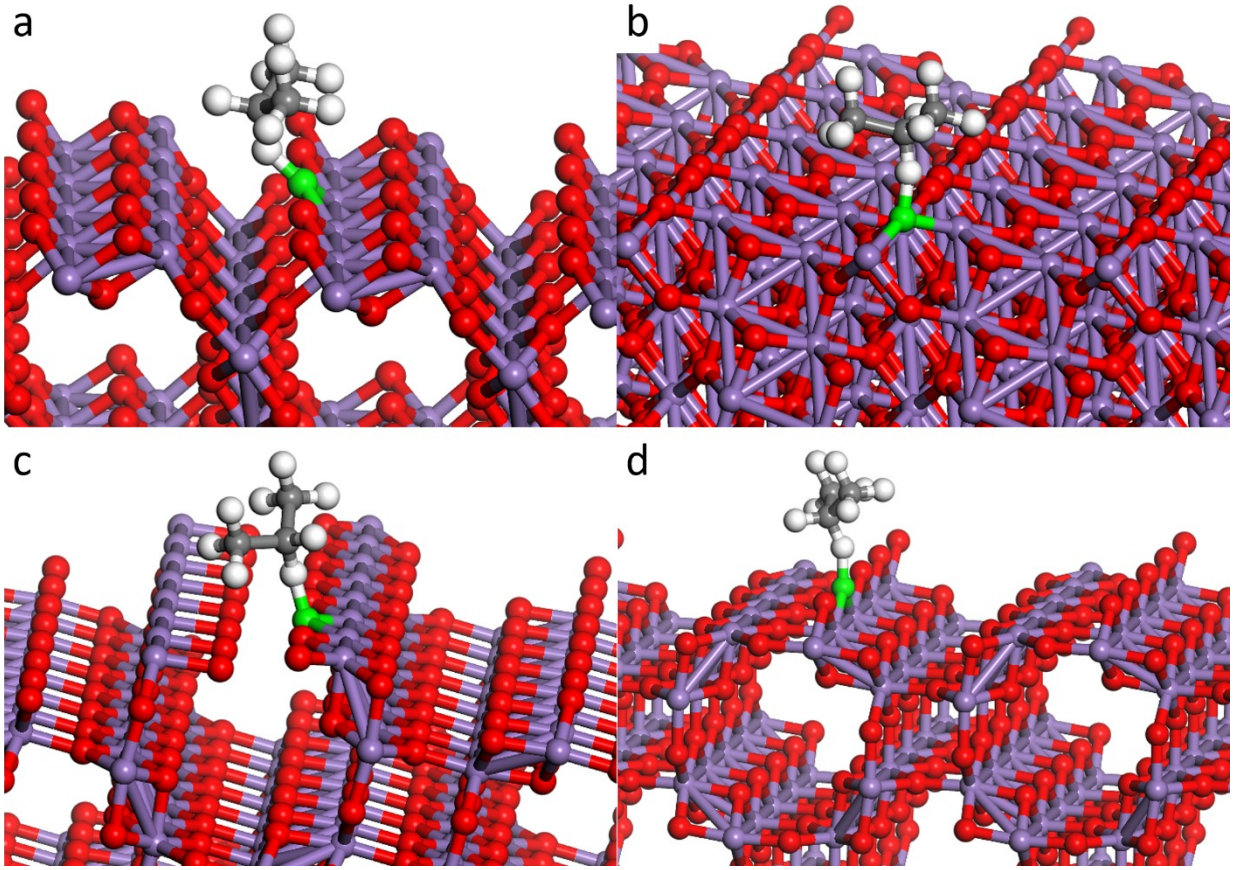


**Figure S11**. Calculated structures of adsorbed propane on (a) $MnO_2$-110, (b) $MnO_2$-211, (c) $MnO_2$-310 and (d) $MnO_2$-200.

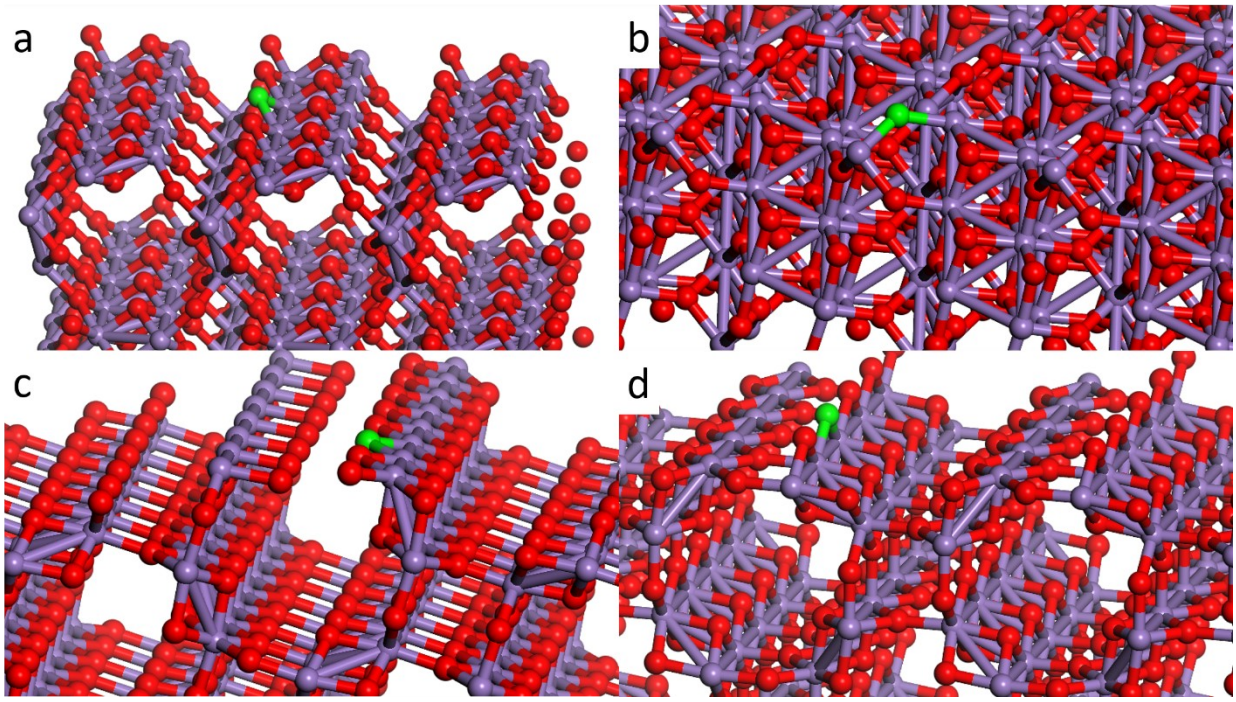


**Figure S12**. Calculated structures of oxygen vacancy on (a) $MnO_2$-110, (b) $MnO_2$-211, (c) $MnO_2$-310 and (d) $MnO_2$-200.

# Table

**Table S1.** Structural parameters of the α-$MnO_2$ nanowire catalysts before and after reaction.

| Sample | Lattice parameters (Å)[a] | Dcrys[b] (nm) | Sample | Lattice parameters (Å)[a] | Dcrys[b] (nm) |
|---|---|---|---|---|---|
| | $MnO_2$ (211) | | | $MnO_2$ (211) | |
| $MnO_2$-110 | 9.8457 | 10.504 | $MnO_2$-110-af | 9.8543 | 10.372 |
| $MnO_2$-211 | 9.8404 | 10.544 | $MnO_2$-211-af | 9.8661 | 10.698 |
| $MnO_2$-310 | 9.8234 | 11.167 | $MnO_2$-310-af | 9.8625 | 11.692 |
| $MnO_2$-200 | 9.8097 | 12.1 | $MnO_2$-200-af | 9.8624 | 12.718 |

[a] calculated from lattice constants from peak locations and miller indices
[b] calculated from the Scherrer formula

**Table S2.** Structural and physical parameters of the α-$MnO_2$ nanowire catalysts.

| **Sample** | **$S_{BET}$ ($m^2 \cdot g^{-1}$)** | **$S_{BJH}$ ($m^2 \cdot g^{-1}$)** | | **$V_p$ ($cm^3 \cdot g^{-1}$)** | **$C_3H_8$ ads(%)** | **$O_2$ ads(%)** |
|---|---|---|---|---|---|---|
| | | $S_{Ads}$ | $S_{Des}$ | | | |
| **$MnO_2$-110** | 49.1 | 37.1 | 55.1 | 0.58 | 0.198 | 0.211 |
| **$MnO_2$-211** | 46.3 | 31.1 | 45.8 | 0.57 | 0.177 | 0.208 |
| **$MnO_2$-310** | 43.4 | 28.5 | 41.8 | 0.55 | 0.149 | 0.198 |
| **$MnO_2$-200** | 41.6 | 28.4 | 38.3 | 0.54 | 0.116 | 0.168 |

**Table S3.** XPS data of α-$MnO_2$ nanowire catalysts before, at $T_{50}$ of and after reaction.

| Sample | Before reaction | | | At $T_{50}$ of reaction | | | After reaction | | |
|---|---|---|---|---|---|---|---|---|---|
| | $Mn^{4+}$% | $Mn^{3+}$% | $Mn^{2+}$% | $Mn^{4+}$% | $Mn^{3+}$% | $Mn^{2+}$% | $Mn^{4+}$% | $Mn^{3+}$% | $Mn^{2+}$% |
| $MnO_2$-110 | 44.97 | 48.38 | 6.65 | 54.12 | 41.74 | 4.13 | 41.18 | 51.56 | 7.26 |
| $MnO_2$-211 | 40.97 | 51.49 | 7.53 | 52.74 | 41.73 | 5.51 | 42.88 | 49.37 | 7.75 |
| $MnO_2$-310 | 36.29 | 47.86 | 15.85 | 47.81 | 44.98 | 7.19 | 43.56 | 46.21 | 10.23 |
| $MnO_2$-200 | 20.06 | 45.60 | 34.34 | 45.08 | 46.67 | 8.23 | 38.36 | 51.13 | 10.51 |
| Sample | Before reaction | | | At $T_{50}$ of reaction | | | After reaction | | |
| | $O_{sur}$ % | $O_{latt}$ % | $O_{sur}/O_{latt}$ | $O_{sur}$ % | $O_{latt}$ % | $O_{sur}/O_{latt}$ | $O_{sur}$ % | $O_{latt}$ % | $O_{sur}/O_{latt}$ |
| $MnO_2$-110 | 28.9 | 71.1 | 0.41 | 28.3 | 71.69 | 0.39 | 29.98 | 70.02 | 0.43 |
| $MnO_2$-211 | 28.79 | 71.01 | 0.40 | 28.17 | 71.82 | 0.39 | 29.31 | 69.69 | 0.42 |
| $MnO_2$-310 | 24.82 | 75.18 | 0.33 | 25.98 | 74.01 | 0.35 | 30.87 | 69.13 | 0.44 |
| $MnO_2$-200 | 22.73 | 77.27 | 0.29 | 25.68 | 74.31 | 0.34 | 30.06 | 69.94 | 0.43 |

**Table S4.** $H_2$-TPR data of α-$MnO_2$ nanowire catalysts.

| Sample | Peak 1 | | Peak 2 | |
|---|---|---|---|---|
| | Position | Percentage | Position | Percentage |
| $MnO_2$-110 | 230.64 | 0.32 | 272.0 | 0.68 |
| $MnO_2$-211 | 237.9 | 0.26 | 275.1 | 0.74 |
| $MnO_2$-310 | 247.5 | 0.22 | 285.5 | 0.78 |
| $MnO_2$-200 | 253.5 | 0.09 | 301.3 | 0.91 |

**Table S5.** $O_2$-TPD data of α-$MnO_2$ nanowire catalysts.

| Sample | Peak 1 | | Peak 2 | | Peak 3 | | Peak 4 | |
|---|---|---|---|---|---|---|---|---|
| | Position | Percentage | Position | Percentage | Position | Percentage | Position | Percentage |
| $MnO_2$-110 | 133.77 | 49.01 | 215.67 | 13.23 | 341.97 | 20.93 | 460.67 | 16.81 |
| $MnO_2$-211 | 139.42 | 44.83 | 217.04 | 9.98 | 346.15 | 29.49 | 482.65 | 15.68 |
| $MnO_2$-310 | 140.41 | 44.39 | 225.21 | 9.99 | 348.07 | 14.78 | 483.91 | 30.82 |
| $MnO_2$-200 | 141.78 | 34.09 | 228.87 | 20.51 | 351.93 | 21.99 | 492.58 | 23.40 |

**Table S6.** Frequencies of functional groups present on the α-$MnO_2$ nanowire catalysts analyzed by DRIFTS

| Mode (wave number $cm^{-1}$) | Infrared band wavenumber ($cm^{-1}$) | | | | References |
|---|---|---|---|---|---|
| | $MnO_2$-110 | $MnO_2$-211 | $MnO_2$-310 | $MnO_2$-200 | |
| $\upsilon_{as}(CH_3)$ | 3040 | 3058 | 3092 | 3078 | [1] |
| $\upsilon_{as}(CH_2)$ | 3000 | 3004 | 3008 | 3012 | [1] |
| $\upsilon_s(C=O)$ | 1720 | 1732 | 1761 | 1755 | [2] |
| $\delta_{as}(HOH)$ | 1650 | 1648 | 1683 | 1660 | [3] |
| $\upsilon_{as}(COO)$ adsorbed on surface | 1524 and 1584 | 1522 and1590 | 1549 and 1619 | 1547 and 1584 | [4] |
| $\upsilon_{as}(COO)$ | 1445 | 1443 | 1448 | 1445 | [5] |
| $\delta_s(CH_3)$ | 1403 | 1389 | 1398 | 1400 | [6] |
| $\upsilon_{as}(C-O)$ | 1307 | 1310 | 1318 | 1297 | [7] |
| $\upsilon_s(CH_3COO)$ | 1258 | 1264 | 1260 | 1232 | [8] |
| $\upsilon_s(C-O-CH)$ | 1202 | 1208 | 1201 | 1180 | [8] |
| $\upsilon_{as}(C-O-C)$ | 1120 | 1096 | 1125 | 1110 | [8] |
| $\upsilon_s(CH-O-CH)$ | 1051 | 1059 | 1059 | 1060 | [8] |

# Reference

[1] Z. Zhao, T. Wu, C. Xiong, G. Sun, R. Mu, L. Zeng and J. Gong, *Angew. Chem. Int. Ed. Engl.*, 2018, **57**, 6791-6795.

[2] B. Wang, X. Wu, R. Ran, Z. Si and D. Weng, *J. Mol. Catal. A: Chem.*, 2012, **361-362,** 98-103.

[3] Y. Jian, X. Feng, M. Tian, Z. Jiang and C. He, *Appl. Surf. Sci.*, 2021, **559,** 149905.

[4] Y. Fang, L. Li, J. Yang, S. Hoang, L. Wang, J. Xu, W. Yang, C. Pan, Y. Zhu, H. Deng, Z. Luo, C. Sun, D. Gao, Z. Li and Y. Guo, *Environ. Sci. Technol.*, 2020, **54,** 15476-15488.

[5] T. Zhang, X. Lang, A. Dong, X. Wan, S. Gao, L. Wang, L. Wang and W. Wang, *ACS Catal.*, 2020, **10,** 7269-7282.

[6] J. Zhao, C. Tu, W. Sun, H. Xia, H. Zhang, Q. Dai and X. Wang, *Catal. Sci. Tech*., 2020, **10,** 742-756.

[7] H. Wang, B. Peng, R. Zhang, H. Chen and Y. Wei, *Appl. Catal. B: Environ.*, 2020, **276,** 118922.

[8] W. Zhu, X. Chen, C. Li, Z. Liu and C. Liang, *J. Catal.*, 2021, **396,** 179-191.